Doping-modulated Strain Control of Bifunctional Electrocatalysis for Rechargeable Zinc-air Batteries

Zhao Li[1,2,#], *Qi Wang*[3,#], *Xiaowan Bai*[4,#], *Maoyu Wang*[5,#], *Zhenzhong Yang*[6], *Yingge Du*[6], *George E. Sterbinsky*[7], *Duojie Wu*[3], *Zhenzhen Yang*[8], *Huajun Tian*[1], *Fuping Pan*[1], *Meng Gu*[3,*], *Yuanyue Liu*[4,*], *Zhenxing Feng*[5,*], *and Yang Yang*[1,2,9,10,*]

[1] *NanoScience Technology Center, University of Central Florida, Orlando, FL 32826, United States*

[2] *Department of Materials Science and Engineering, University of Central Florida, Orlando, FL 32826, United States*

[3] *Department of Materials Science and Engineering, Southern University of Science and Technology, Shenzhen 518055, China*

[4] *Texas Materials Institute and Department of Mechanical Engineering, The University of Texas at Austin, Austin, Texas 78712, USA.*

[5] *School of Chemical, Biological, and Environmental Engineering, Oregon State University, Corvallis, OR 97331, United States*

[6] *Physical and Computational Sciences Directorate, Pacific Northwest National Laboratory, Richland, Washington 99352, United States*

[7] *X-ray Science Division, Advanced Photon Source, Argonne National Laboratory, 9700 S Cass Avenue, Argonne, IL, 60439, United States*

[8] *Chemical Sciences and Engineering Division, Argonne National Laboratory, 9700 S Cass Avenue, Lemont, IL, 60439, United States*

[9] *Renewable Energy and Chemical Transformation Cluster, University of Central Florida, Orlando, FL 32826, United States*

[10] *Department of Chemistry, University of Central Florida, Orlando, FL 32826, United States*

[*] *Email: gum@sustc.edu.cn; zhenxing.feng@oregonstate.edu; Yuanyue.liu@austin.utexas.edu; Yang.Yang@ucf.edu*

[#] *These authors contributed equally to this work.*

Abstract

Changes in the local atomic arrangement in crystal caused by the lattice-mismatch-induced strain can efficiently regulate the performance of zinc-air batteries (ZABs) electrocatalysts in many manners, mainly due to modulated electronic structure configurations that affect the adsorption energies for oxygen-intermediates formed during oxygen reduction and evolution reactions (ORR and OER). However, the application of strain engineering in electrocatalysis has been frustrated by strain relaxation caused by structural instability such as dissolution and destruction, leading to insufficient durability towards ORR/OER. Herein, we propose a doping strategy to modulate the phase transition and formation of self-supported cobalt fluoride-sulfide (CoFS) nanoporous films using a low amount of copper (Cu) as a dopant. Such a well-defined Cu-CoFS heterostructure overcomes the obstacle of structural instability. Our study of the proposed Cu-CoFS also helps establish the structure-property relationship of strained electrocatalysts by unraveling the role of local strain in regulating the catalyst electronic structure. As a proof-of-concept, the Cu-CoFS electrocatalyst with doping-modulated strain exhibited superior onset potentials of 0.91 V and 1.49 V for ORR and OER, respectively, surpassing commercial Pt/C@RuO_2 and benchmarking non-platinum group metals (non-PGMs) catalysts. The ZABs with Cu-CoFS catalyst delivered an excellent charge/discharge cycling performance with an extremely low voltage gap of 0.5 V at the current density of 10 mA cm^{-2} and successively 0.93 V under high current density 100 mA cm^{-2} and afforded an outstanding peak power density of 255 mW cm^{-2}.

Keywords: local strain; lattice mismatch; heterostructure; electrocatalysis; zinc-air battery

TOC

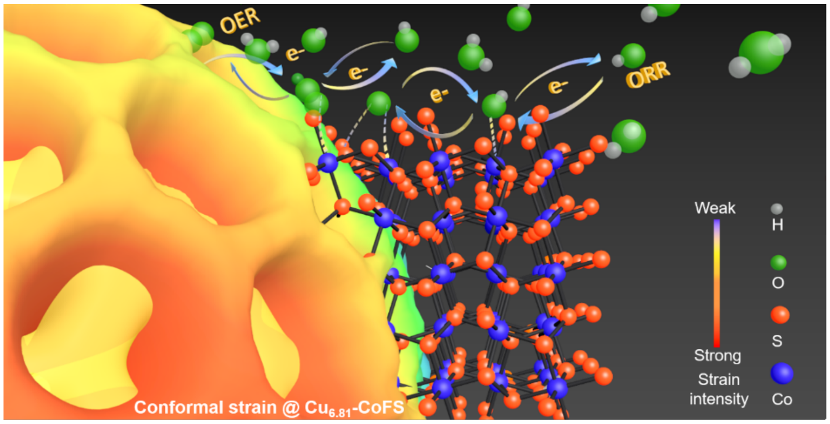

TOC entry: A new strategy is designed to synthesize the strained cobalt fluoride-sulfide (CoF_2-CoS_2, denoted as CoFS) catalysts with tunable lattice strains modulated by the Cu-dopant and stabilized local strain by forming core-shell heterostructure in the well-confined porous/tubular CoFS films.

Broader Context: A new understanding of the rational design of efficient electrocatalysts by strain engineering for renewable energy and catalysis is provided in this work. Also, the strain-catalysis relationship is further understood by investigating the bifunctional oxygen reduction and evolution reactions (ORR and OER) activities that have been recognized to be sluggish because of the 4-electron transfer process. The proposed doping-modulated strain control in the well-defined heterostructured materials can be applied to broader fields where the localized strain plays a crucial role in realizing the performance improvement, including but not limited to quantum photonics, superconductor science, intelligent electronics, and beyond. This work is presented across different disciplines, including Catalysis, Material Science, and Electrochemistry.

1. Introduction

Propelled by the ever-increasing global energy crisis and climate change, renewable energy technologies such as metal-air batteries have attracted widespread research interest.[1-4] Particularly, rechargeable zinc-air batteries (ZABs) with high energy, zero-emission, and low cost, driven by reversible oxygen redox electrocatalysis, are among the most promising candidates to realize renewable energy initiatives.[5, 6] The electrocatalytic efficiency for oxygen reduction and evolution reactions (ORR and OER) should be optimized to achieve the preeminent ZABs performance in practice. Unfortunately, the sluggish 4-electron transfer process for ORR/OER always results in low efficiency and high overpotential to reach expected reaction rates.[7] Presently, platinum group metals (PGMs) are considered as the benchmarking ORR/OER catalysts for ZABs, due to their preferable electronic structures and optimized adsorption energy of reaction intermediates.[1, 3] However, the high cost and low abundance of PGMs impede their widespread usage in ZABs. In addition, catalyst deactivation caused by structural instability is another challenge, leading to the increased voltage hysteresis of ZABs during cycling. Thereupon, a highly reversible oxygen catalyst with excellent stability and low cost is of considerable interest for ZABs.

According to the Sabatier principle, an optimal ORR/OER catalyst should have a proper binding strength of the reaction intermediates (*OOH, *O, and *OH) with the active sites, which should be neither too strong nor too weak.[7] Recent studies have suggested that the lattice strain, either compressive or tensile, can be adopted to tailor the intermediate binding strength,[8] as well as regulating the electronic configuration of transition metal cations to improve the catalytic activity.[9-12] Conventionally, strain engineering can be realized by the external perturbations from a heterogeneous substrate or external pressure.[12-16] However, the strain relaxation caused by the structural instability (i.e., element dissolutions, morphology/composition reconstructions, mechanical failures, etc.) compromises the benefits of strain-induced catalysis enhancement.[17] Particularly, the element dissolution (composition degradation) and the morphology change (e.g., surface reconstruction and aggregation) are inescapable under long-term operating conditions.[11, 18, 19] As a result, the primitive strain can be subject to relaxation. In addition, the formation and propagation of cracks that are susceptible to less constrained bonds could continuously cause an irreversible consequence in strain instability.[20] All these structural instability issues would be huge impediments on the strain engineering and thus lead to insufficient durability of catalytic performance. Thus, implementation of new methods to effectively generate and stabilize the local strain in the electrocatalysts to optimize their electronic configurations and catalytic activities in a controllable and reliable manner is of critical importance.[9, 21, 22]

Transition metal chalcogenides (TMC) have gained rising attention as non-PGMs electrocatalysts due to their tunable electronic structures and earth abundance.[10, 23, 24] Particularly, cobalt sulfide (CoS_2) as a representative of TMC shows enhanced ORR/OER activities due to its sensitivity to the strong electronic coupling at the heterogeneous interface,[25-28] which could be an ideal model material to study the local strain effect on catalysis. To address the above-mentioned structural instability issues of strained catalysts, the concept proposed herein is to design a self-supported cobalt fluoride-sulfide (CoF_2-CoS_2, denoted as CoFS) nanoporous film, in which a low amount of copper (Cu) is used to promote the CoF_2-CoS_2 phase transition and thus modulate the lattice strain initiated at the two-phase interface. More specifically, CoS_2 is present on the surface of the proposed Cu-CoFS, serving as a catalytic phase for ORR/OER. The local strain originating from the lattice mismatch and innate coupling of CoF_2-CoS_2 can be effectively modulated to tune the electronic configuration of Co cation for catalysis. The Cu-dopant is proposed to adjust the two-phase ratio of CoF_2-CoS_2, which plays an essential role in modulating the lattice strain initiated at the two-phase interface. Furthermore, our prior studies suggest that the well-defined nanoporous structure of the catalyst enables unique features that provide substantial improvements in electrochemical performance, including but not limited to open channels that facilitate mass transport, an absence of additives to avoid interference from carbonaceous materials, and strong adhesion to the substrates endowing the catalyst with reduced Ohmic resistance and enhanced structural stability.[29] Overall, the proposed Cu-CoFS is a favorable platform for establishing the relationship between strain, electronic structure, and catalytic activity. It can also ensure keeping the structural integrity of the nanostructure for long-term ZABs cycling under harsh conditions. As a proof-of-concept, superior onset potentials of 0.91 V and 1.49 V for ORR and OER, respectively, are achieved with an excellent charge/discharge cycling performance with an extremely low voltage gap of 0.5 V at the current density of 10 mA cm^{-2} and successively 0.93 V under high current density 100 mA cm^{-2} as well as an outstanding peak power density of 255 mW cm^{-2}. When used in foldable ZABs, Cu-CoFS also shows outstanding stability during bending tests, revealing a promising candidate for wearable devices.

2. Results and Discussion

The procedure for synthesizing Cu-CoFS nanoporous films is illustrated in **Figure 1**a. First, thin layers of freestanding metallic Co films incorporating variable amounts of Cu-dopant (Cu-Co) were fabricated via an electrodeposition approach (more details in Supplementary Information). Subsequently, the anodic treatment in fluorine (F)-containing electrolyte was adopted to convert/fluorize metallic Cu-Co films to Cu-doped CoF_2 (Cu-CoF_2) nanoporous films. Afterward, a sulfurization process was used to perform the CoF_2-CoS_2 phase transition, eventually forming nanoporous Cu-CoFS films with a controlled two-phase interface. The Cu content in Cu_x-CoFS (x = 0, 4.42, 6.81, and 11.27 at%, denoted as CoFS, $Cu_{4.42}$-CoFS, $Cu_{6.81}$-CoFS, and $Cu_{11.27}$-

CoFS, respectively) was quantified by X-ray fluorescence spectrometer (XRF). From scanning electron microscopy (SEM) images shown in **Figure S1-2**, the Cu_x-CoFS nanoporous films with different Cu contents showed an interconnected channel-like network with highly ordered and open pores (average pore size of ~200 nm), making the interior surfaces of the catalysts accessible for electrochemical reactions.[30] The cross-sectional SEM images also reveal the self-supported tubular channels seamlessly connected to the underlying substrate (residual metallic Co), suggesting a strong adhesion and adequate charge transfer at the substrate/catalyst interface, as well as a facilitated mass transport inside these open channels.[31]

X-ray diffraction (XRD) analysis was employed (**Figure S3**) to understand the phase transition from CoF_2 to the heterostructured CoFS with Cu-doping. The diffraction peaks at 34.08°, 39.13°, 52.26°, and 54.92° suggest the successful formation of CoF_2 in a tetragonal structure (space group P42/mnm) after anodization. After sulfurization treatment, the characteristic diffraction peaks of CoS_2 in the cubic Pa-3 space group appear, which indicates the successful formation of a two-phase CoF_2-CoS_2 heterostructure. Moreover, to gain an insightful understanding of the local strain induced by the lattice mismatch inside Cu_x-CoFS, the corresponding fine structures were investigated by high-resolution transmission electron microscopy (HRTEM). As demonstrated in the HRTEM image of CoFS (no Cu-doping, **Figure S4**), slight lattice distortion was observed at the interface between CoF_2 and CoS_2 nanodomains. With the incorporation of Cu-dopant in the CoFS matrix, the distortion is homogeneously distributed across the whole film. This reveals the critical role of Cu in controlling the formation of the CoF_2-CoS_2 heterostructure, which in turn generates local strain across the entirety of the catalyst.

Aberration-corrected high-angle annular dark-field scanning TEM (HAADF-STEM) images (**Figure 1**b-f) were employed to have a further understanding of the local strain generation in the heterostructures by examining the atomic arrangement of Cu_x-CoFS. The corresponding atomic model of CoS_2 is presented in **Figure 1**e, which is consistent with the obtained CoS_2 phase in Cu_x-CoFS viewed along the [110] direction in **Figure 1**b-d. The lattice spacings of CoS_2 (200) facets for $Cu_{4.42}$-CoFS (2.55 Å), $Cu_{6.81}$-CoFS (2.64 Å), and $Cu_{11.27}$-CoFS (2.68 Å) are smaller than that of standard CoS_2 (2.769 Å), showing a compressive strain along the [001] direction. Viewing from another direction of the facet, the lattice spacings also show compressive strain along the [010] direction (**Table S1**), which proves the existence of lattice strain in CoS_2. The lattice mismatch and distortion of $Cu_{6.81}$-CoFS were further examined by the HAADF-STEM imaging. The image in **Figure 1**f shows two tetragonal CoF_2 nanodomains separated by a cubic CoS_2 nanodomain in the middle, which agrees well with the co-existence of both phases illustrated in the XRD patterns. Moreover, the corresponding geometric phase analysis (GPA, **Figure 1**g) was applied to record the variation in the lattice parameter and the lattice strain distribution in the nanodomains, proving that the lattice-mismatch-induced strain was initiated at the CoF_2-CoS_2 interface.

Element distributions of $Cu_{6.81}$-CoFS recorded by STEM-electron energy-loss spectroscopy (EELS) mapping (**Figure 1**h) confirm the existence of S in the outside periphery (i.e., CoS_2) and F primarily in the inside skeleton (i.e., CoF_2) of the tubular heterostructures. The CoF_2 cores could be considered as efficient agents in the manipulation and stabilization of the lattice strains in the CoS_2 shells. Besides, Cu was evenly distributed throughout the whole material, serving as an efficient agent to promote CoF_2-CoS_2 phase transition and to modulate the two-phase interface in the heterostructured Cu_x-CoFS.

Spectroscopic methods, including X-ray photoelectron spectroscopy (XPS), ultraviolet photoelectron spectroscopy (UPS), and X-ray absorption spectroscopy (XAS), were employed to elucidate the chemical states and electronic structures of the strained $Cu_{6.81}$-CoFS and other control samples. First, the high-resolution XPS spectra (**Figure S5**a) of Co 2p characteristic peaks at 778.83 (Co 2p3/2) and 793.65 eV (Co 2p1/2) are spin-orbit peaks assigned to CoS_2 in the Cu_x-CoFS.[32, 33] The XPS Cu 2p peaks for Cu^{2+} in the Cu_x-CoFS (**Figure S5**b) show that the Cu-dopants are successfully incorporated into the heterostructure.[34] The XPS F 1s peak for the Cu_x-CoFS (**Figure S6**) located at approximately 685 eV belongs to the Co-F bond.[35, 36] The XPS S 2p peaks (**Figure 2**a) show two pairs of doublets at 162.80/163.97 eV and 161.3/162.5 eV, which are the characteristic S_2^{2-} and S^{2-} in the TMC, respectively.[37, 38] The peak at 164.69 eV is most likely from the surface adsorbed sulfur residuals after sulphurization treatment.[39] Note that the S/F ratio as estimated in **Table S2** increases with the Cu content in the Cu_x-CoFS, indicating a prompted phase transition from CoF_2 to CoS_2 achieved by adding Cu-dopant.[40] Moreover, UPS results (**Figure 2**b and **Figure S7**) provide a deep understanding of the role of lattice strain in regulating the electronic configuration of Cu_x-CoFS. The work function of $Cu_{6.81}$-CoFS is about 4.55 eV, which is lower than those of CoFS (5.02 eV), $Cu_{4.42}$-CoFS (4.87 eV), and $Cu_{11.27}$-CoFS (4.79 eV). It reveals that the compressive strain modulated by Cu-doping through control of the CoF_2-CoS_2 phase transition and strain distribution at the two-phase interface is favorable for optimizing the electronic structure of Cu_x-CoFS. Furthermore, the decreased work function of $Cu_{6.81}$-CoFS is very likely to contribute to the enhanced reaction rates for the catalytic processes.[41] Meanwhile, XAS was carried out to understand the critical role of Cu-doping-modulated strain in regulating the electronic structure of Cu_x-CoFS.[42-44] X-ray absorption near edge structure (XANES) of Cu K-edge (**Figure 2**c) and Co K-edge (**Figure 2**d) spectra show that Cu and Co cations in different Cu_x-CoFS have oxidization states similar to $Cu^{2+}$and Co^{2+}, respectively,[45, 46] consistent with the XPS results. Moreover, the intensity of the Co white line peak (7725 eV) decreases first and then increases with increasing Cu-dopant content. While the changes in the intensity of the Cu white line peak (9000 eV) show the opposite trend. Those changes could correspond to the changes in empty states and the electronic structure.[47, 48] The $Cu_{6.81}$-CoFS shows the most empty Co states and the least empty Cu states in the Cu_x-CoFS samples. Note that CoF_2 has the highest white line intensity, and CoS_2 has the lowest white line intensity. The white line intensity changes of Cu_x-CoFS samples suggest that the Cu-dopant modifies the ratio of Co-F and Co-S bonding. Adding Cu helps the formation of Co-S, which is also confirmed by Cu and Co K-edge extended X-ray absorption fine structure (EXAFS) spectroscopy for Cu_x-CoFS (**Figure 2**e-f and **Figure S8**). In the Cu K-edge EXAFS Fourier transform magnitude, the peak around 1.8 Å could be the mixture of Cu-F and Cu-S bonding comparing with standard Cu-F bond (1.4 Å) in $CuCoF_2$ and Cu-S bond (1.9 Å) in Cu-CoS_2 (**Figure 2**e). The peak position in Cu_x-CoFS moves to a higher radial distance compared to Cu-CoF_2, suggesting that the Cu-dopant could weaken its bonding with F by forming the bonding with S. In contrast, the first peak around 1.75 Å in the Co K-edge EXAFS (**Figure 2**f) should consist of Co-F and Co-S bonds, but a strong Co-F constituent in Cu_x-CoFS indicates the difficulty to break Co-F bond. Precisely, the average bonding distances for Cu_x-CoFS increase comparing to CoFS and the $Cu_{6.81}$-CoFS has the longest average bonding distance (**Figure 2**f). These results further confirm that the Cu-dopant could help the CoF_2-CoS_2 phase transition by creating an enriched coordination environment for Co when sulfurization takes place.

Electrochemical ORR performance of Cu_x-CoFS and control samples (CoFS and commercial Pt/C@RuO_2) were evaluated in a typical three-electrode setup with 0.1 M KOH electrolyte. From cyclic voltammograms (CV, **Figure S9**), the Cu_x-CoFS catalysts show more positive onset potentials for ORR in the O_2-saturated electrolyte compared with CoFS. Among these Cu_x-CoFS catalysts, the $Cu_{6.81}$-CoFS possesses the best performance in terms of onset potential and ORR peak current. From linear sweep voltammograms (LSV, **Figure S9**a), the $Cu_{6.81}$-CoF also exhibits supreme ORR performance (i.e., onset potential of 0.91 V, half-wave potential $E_{1/2}$ of 0.80 V, the diffusion-limited current density of 5.86 mA cm^{-2} at 0.4 V), superior to those of CoFS, $Cu_{4.42}$-CoFS, $Cu_{11.27}$-CoFS, and surpassing those of commercial Pt/C@RuO_2 and benchmarking non-PGMs catalysts (**Table S3**). Furthermore, the LSV curves tested at different rotation speeds (**Figure S10**b and **Figure S11**b,d,f,h) and the corresponding Koutecky-Levich (K-L) plots (**Figure S10**c and **Figure S11**a,c,e,g) for all samples were recorded to examine their intrinsic ORR activities. Electron transfer number (n) of almost 4 was estimated for $Cu_{6.81}$-CoFS from the slope of K-L plots, suggesting a more favorable four-electron ORR process than other control samples (n = 2.89, 3.15, and 3.89 for CoFS, $Cu_{4.42}$-CoFS, and $Cu_{11.27}$-CoFS, respectively) and comparable to commercial Pt/C@RuO_2 (~4). Electrochemically active surface areas (ECSA) of the catalysts estimated from the double-layer capacitance (**Figure S10**d) are approximately 0.014 mF cm^{-2}, 0.015 mF cm^{-2}, 0.021 mF cm^{-2}, and 0.016 mF cm^{-2} for CoFS, $Cu_{4.42}$-CoFS, $Cu_{6.81}$-CoFS, and $Cu_{11.27}$-CoFS, respectively. A reduced charge transfer resistance for $Cu_{6.81}$-CoFS compared with other control samples was obtained from electrochemical impedance spectroscopy (EIS, **Figure S12**), suggesting the facilitated charge transfer and optimized electronic structure of $Cu_{6.81}$-CoFS for catalysis by the Cu-doping-modulated strain.

The electrochemical OER activities of all samples were also examined by the LSV curves recorded in 0.1 M KOH electrolyte (**Figure S13**a). The overpotentials at the current density of 10 mA cm^{-2} (η_{10}) decrease from 37 mV (CoFS) to 35 mV ($Cu_{4.42}$-CoFS), 31 mV ($Cu_{6.81}$-CoFS), and 32 mV ($Cu_{11.27}$-CoFS), confirming the outstanding OER performance of Cu_x-CoFS compared with commercial Pt/C@RuO_2 and the state-of-the-art catalysts (**Table S3**). The $Cu_{6.81}$-CoFS catalyst displays a smaller Tafel slope of 88 mV dec^{-1} (**Figure S13**b) than CoFS (98 mV dec^{-1}), $Cu_{4.42}$-CoFS (93 mV dec^{-1}), and $Cu_{11.27}$-CoFS (90 mV dec^{-1}), due to the accelerated electron transfer.

The potential gap ΔE ($\Delta E = E_{j=10} - E_{1/2}$, where $E_{j=10}$ is the potential at 10 mA cm^{-2} for OER and $E_{1/2}$ is the half-wave potential for ORR, **Figure 3**a) was estimated to evaluate the overall performance of the catalysts for ZABs. The $Cu_{6.81}$-CoFS delivers the smallest gap of 0.74 V towards ORR/OER, in comparison with other control samples (CoFS: 0.83 V, $Cu_{4.42}$-CoFS: 0.80 V, $Cu_{11.27}$-CoFS: 0.76 V, and commercial Pt/C-RuO_2: 0.82 V), which also surpasses the benchmarking electrocatalysts (**Table S3**). To further evaluate the electrochemical stability of Cu_x-CoFS, chronoamperometric tests were performed in 0.1 M KOH. Noticeably, the $Cu_{6.81}$-CoFS shows a significantly improved stability for long-term usage over 40,000s (**Figure S14**) compared with commercial Pt/C@RuO_2, CoS_2, and CoFS (**Figure S15**), suggesting the supreme durability for ZABs applications.

The assessment of $Cu_{6.81}$-CoFS was first performed by assembling it into ZABs operated in a static state (without electrolyte flow) and comparing it with commercial Pt/C@RuO_2. The galvanostatic charge/discharge cycling was recorded at the current densities of 5 and 10 mA cm^{-2} for $Cu_{6.81}$-CoFS (**Figure S16**) to explore the reversibility during long-term cycling. Remarkably, the $Cu_{6.81}$-CoFS shows low voltage hysteresis of 0.81 V and 0.89 V at 5 and 10 mA cm^{-2}, respectively, which remain unchanged without any degeneration after 240h cycling. Note that commercial Pt/C@RuO_2 (**Figure S17**) shows the voltage hysteresis increase from 0.90 V to 1.91 V after only 30h testing at the current density of 10 mA cm^{-2}, indicating catalyst deactivation during cycling. We further tested the cycling performance of $Cu_{6.81}$-CoFS in ZABs in a dynamic state with electrolyte flow, which can help to alleviate the surface passivation of the electrodes and reduce the mass transport barrier for the catalytic reactions.[6, 49] A drastically reduced voltage hystereses of approximately 0.50 V and 0.93 V were successively achieved at 10 and 100 mA cm^{-2} (**Figure 3**b), operating for 480 h cycling, respectively, superior to the state-of-the-art ZABs.[3, 50,

[51] The discharging rate performance of $Cu_{6.81}$-CoFS tested in ZAB flow cells at current densities from 5 to 100 mA cm^{-2} (**Figure S18**) show excellent stability at each discharge current and exhibit high output voltages ranging from 1.43 to 1.0 V. The polarization curves (**Figure 3**c) show that the $Cu_{6.81}$-CoFS affords a maximal power density of 255 mW cm^{-2} at 535 mA cm^{-2}, which is much higher than that of commercial Pt/C@RuO_2 (102 mW cm^{-2} at 225 mA cm^{-2}) and superior to the state-of-art ZABs (**Table S4**).

To verify our catalyst as a favorable electrode with excellent stability, the structural and compositional characterizations of $Cu_{6.81}$-CoFS after ZABs cycling were performed. The attention is mainly focused on morphology integrity and local structural stability. First of all, as illustrated in SEM images (**Figure S19**), the nanoporous structure of $Cu_{6.81}$-CoFS with an interconnected channel-like network is well maintained after the ZABs cycling. It proves that the well-defined $Cu_{6.81}$-CoFS possesses excellent structural integrity without destruction. Then, corresponding high-resolution TEM images and XANES/EXAFS (K space) of Co and Cu K-edge attributing to $Cu_{6.81}$-CoFS after reactions were recorded, aiming to determine the local structural stability, particularly the existence of strain inside our heterostructure. As illustrated in **Figure S20**, the relatively smaller lattice spacing around 2.65 Å compared with the standard CoS_2 (2.769 Å), confirms the existence of compressive strain for $Cu_{6.81}$-CoFS after reactions. It keeps well as the pristine one shown in **Figure 1c** confirming the stability of our catalyst structure. Besides, the well survived lattice-mismatched interfaces inside the sidewall of the $Cu_{6.81}$-CoFS tubular channel further reveals its vital contribution to keeping local strained CoS_2 and avoiding strain relaxation for the entirety of the catalyst. Moreover, the XAS results in **Figure S21** are similar to those before the battery tests. It suggests that careful two-phase controlled $Cu_{6.81}$-CoFS heterostructure can maintain the favorable bonding strength among Co-F/Co-S and Cu-F/Cu-S and realize corresponding robustness with negligible strain relaxation.

The $Cu_{6.81}$-CoFS electrode was also assembled into foldable solid-state ZABs to seek potential applications for portable and wearable electronics because of its mechanically robust and freestanding structure under twisting and folding (**Figure S22**). The foldable ZABs display an open-circuit potential (OCP) of 1.44 V (**Figure S23**) before bending. The bending test of the foldable ZABs was performed at 1 mA cm^{-2} under various bending angles (**Figure 3**d), showing almost no voltage change under various deformations. Particularly, the foldable ZABs delivered sufficient energy to power personal electronics, taking an electric fan as an example (**Figure 3**e and **Video S1-4**), under different bending states. Besides, the foldable ZABs maintained stable performance over 30 h cycling (**Figure S24**), as well as stable rate performance in the current density range from 0.5 to 10 mA cm^{-2} (**Figure S25**), confirming the prominent reversibility for practical applications.

Density functional theory (DFT) calculations were conducted to thoroughly understand the oxygen electrochemistry for the strained $Cu_{6.81}$-CoFS and the correlation between the Cu-doping-modulated strain and ORR/OER activities. The CoS_2(100) facet was chosen to study the origin of ORR/OER activity with strain states from -8% (compressive) to 3% (tensile) generated in both [010] and [001] crystal directions, consistent with the TEM results (**Figure 1**). The configurations, corresponding energies, and Co−O bond lengths of intermediates involved in ORR/OER are listed in **Table S6**. The calculated results show that *OOH and *OH species prefer to be adsorbed at the top site of Co atoms, and the bond length of Co-O decreases monotonously with increasing strain. However, the adsorption of *O changes from the bridge site between Co and O to the top site of Co, due to the increase in the bond length of Co-S as the lattice strain increases. Moreover, the overall ORR/OER pathway was calculated under the different lattice strains, and the free energy diagrams are shown at the equilibrium potential (U_0(RHE) =1.23 V, **Figure 4**a). Evidently, the rate-determining step (RDS) is switched from $*O + H_2O(l) + e^- \rightarrow *OH + OH^-$ to $*OH + e^- \rightarrow * + OH^-$ by changing the compressive strain to tensile strain with the theoretical overpotentials of 0.50, 0.33, 0.39, 0.46, and 0.51 V for the strains of -8%, -6%, -3%, 0%, and 3%, respectively. The changing trend of the theoretical overpotentials in ORR is consistent with the experimental results (**Figure 4**b). Furthermore, a shift of the d band center (ε_d) to a higher energy level was observed with increasing the lattice strain (**Figure 4**c), implying that the adsorption energy of *OOH, *O, and *OH increases with lattice strain.[52] This result confirms that the lattice strain can optimize the 3d orbital occupation of Co^{2+}, thus resulting in a moderate adsorption strength of the intermediates. Accordingly, the possible four-electron transfer paths for ORR/OER (**Figure 4**d) are proposed, where O_2 first combines with the H_2O molecule to form *OOH, then further reduces to *O and *OH, and finally desorbs from the surface in the form of OH^- (for ORR), while OER proceeds in the reverse direction. The above calculation results confirm that a moderate compressive strain can effectively improve the ORR/OER performance, while over-compressive strain or tensile strain can lead to decreased catalytic activity, highly consistent with the experimental results.

3. Conclusion

In summary, we have designed a facile strategy to controllably synthesize the strained catalysts with tunable lattice strains modulated by the Cu-dopant and stabilized local strain by forming core-shell heterostructure in the well-confined porous/tubular films, free from strain relaxation. Consequently, the enhanced and stabilized ORR/OER activities were achieved because of the optimized adsorption energy of intermediates. Particularly, with properly controlling the strain states, the $Cu_{6.81}$-CoFS catalyst permits desirable catalytic performance, setting a state-of-the-art flag for ZABs at the level of practical implementation including a long cyclability over 480 h at both low (10 mA cm^{-2}) and high current densities (100 mA cm^{-2}) and a peak power density of 255 mW cm^{-2}. Overall, this work provides a new understanding of the rational design of efficient electrocatalysts by strain engineering for renewable energy and catalysis. The proposed doping-modulated strain control in the well-defined heterostructured materials can be applied to broader fields where the localized strain plays a crucial role in realizing the performance improvement, including but not limited to quantum photonics,[53] superconductor science,[54] intelligent electronics,[55] and beyond.

Supporting Information

The Supporting Information is available free of charge on the publisher's website. Materials and electrochemical characterizations.

Competing Interests

The authors declare no competing interests.

Author Contributions

Y.Y. led the project. Z.L. designed and performed the experiments and analyzed the data. Q.W., D.W., Z.Y., Y.D., and M.G. took and analyzed the TEM images. X.B. and Y.L. performed the DFT calculations. Z.Y., H.T., and F.P. helped in analyzing the materials. M.W., G.E.S., and Z.F. performed the XAS characterizations and analyzed the data. Z.L. and Y.Y. wrote the paper. All authors discussed the results and revised the paper.

Acknowledgments

This work is funded by the University of Central Florida through a startup grant (20080741). Y.Y. and Z.F. acknowledge financial support from the National Science Foundation under Grant No. CBET-1949840 and CBET-1949870, respectively. The XPS test was supported by the NSF MRI

XPS: ECCS: 1726636, hosted in MCF-AMPAC facility, MSE, CECS, UCF. The XAS measurements were carried out at beamline 9-BM of Advanced Photon Source at Argonne National Laboratory. The use of Advanced Photon Source (APS) of Argonne National Laboratory (ANL) for synchrotron measurements is supported by the Department of Energy under Contract No. DE-AC02-06CH11357. Y.D. acknowledges the support by the U.S. Department of Energy, Office of Science, Office of Basic Energy Sciences, Early Career Research Program under award #68278. Y.L. acknowledges the support of the National Science Foundation (Grant No. 1900039, 2029442) and the Welch Foundation (Grant No. F-1959-20180324). This work used computational resources provided by National Renewable Energy Laboratory, the Extreme Science and Engineering Discovery Environment (XSEDE) through allocation TG-CHE190065 and the Center for Nanoscale Materials (a DOE Office of Science user facility supported under Contract No. DE-AC02-06CH11357) at ANL. M.G. wants to acknowledge Shenzhen Science and Technology Program(Grant No.KQTD20190929173815000), Guangdong Innovative and Entrepreneurial Research Team Program (Grant No. 2019ZT08C044).

References

1. Z. Li, W. Niu, Z. Yang, N. Zaman, W. Samarakoon, M. Wang, A. Kara, M. Lucero, M. V. Vyas and H. Cao, *Energy Environ. Sci.* 2020,**13**, 884
2. W. Niu, S. Pakhira, K. Marcus, Z. Li, J. L. Mendoza-Cortes and Y. Yang, *Adv. Energy Mater.*, 2018, **8**, 1800480.
3. M. Luo, Z. Zhao, Y. Zhang, Y. Sun, Y. Xing, F. Lv, Y. Yang, X. Zhang, S. Hwang, Y. Qin, J.-Y. Ma, F. Lin, D. Su, G. Lu and S. Guo, *Nature*, 2019, **574**, 81-85.
4. Z. Li, W. Niu, Z. Yang, A. Kara, Q. Wang, M. Wang, M. Gu, Z. Feng, Y. Du and Y. Yang, *Energy Environ. Sci.*, 2020, **13**, 3110-3118.
5. C. Guan, A. Sumboja, H. Wu, W. Ren, X. Liu, H. Zhang, Z. Liu, C. Cheng, S. J. Pennycook and J. Wang, *Adv. Mater.*, 2017, **29**, 1704117.
6. J. Fu, Z. P. Cano, M. G. Park, A. Yu, M. Fowler and Z. Chen, *Adv. Mater.*, 2017, **29**, 1604685.
7. A. R. Zeradjanin, *Curr. Opin. Electrochem.*, 2018, **9**, 214-223.
8. J. R. Petrie, V. R. Cooper, J. W. Freeland, T. L. Meyer, Z. Zhang, D. A. Lutterman and H. N. Lee, *J. Am. Chem. Soc.*, 2016, **138**, 2488-2491.
9. Y. Tong, Y. Guo, P. Chen, H. Liu, M. Zhang, L. Zhang, W. Yan, W. Chu, C. Wu and Y. Xie,

Chem, 2017, **3**, 812-821.
10. P. Chen, Y. Tong, C. Wu and Y. Xie, *Acc. Chem. Res.*, 2018, **51**, 2857-2866.
11. M. Luo and S. Guo, *Nat. Rev. Mater.*, 2017, **2**. 17059
12. R. P. Jansonius, L. M. Reid, C. N. Virca and C. P. Berlinguette, *ACS Energy Lett.*, 2019, **4**, 980-986.
13. T. Wu, M. Sun and B. Huang, *InfoMat*, 2020, **2**, 715-734.
14. Y. Chen, Y. Lei, Y. Li, Y. Yu, J. Cai, M.-H. Chiu, R. Rao, Y. Gu, C. Wang and W. Choi, *Nature*, 2020, **577**, 209-215.
15. X. Liu, L. Zhang, Y. Zheng, Z. Guo, Y. Zhu, H. Chen, F. Li, P. Liu, B. Yu, X. Wang, J. Liu, Y. Chen and M. Liu, *Adv. Sci. (Weinh)*, 2019, **6**, 1801898.
16. J. Huang, Y. Jiang, T. An and M. Cao, *J. Mater. Chem. A*, 2020, **8**, 25465-25498.
17. H. Wang, S. Xu, C. Tsai, Y. Li, C. Liu, J. Zhao, Y. Liu, H. Yuan, F. Abild-Pedersen and F. B. Prinz, *Science*, 2016, **354**, 1031-1036.
18. M. Escudero-Escribano, P. Malacrida, M. H. Hansen, U. G. Vej-Hansen, A. Velázquez-Palenzuela, V. Tripkovic, J. Schiøtz, J. Rossmeisl, I. E. Stephens and I. Chorkendorff, *Science*, 2016, **352**, 73-76.
19. M. Escudero-Escribano, A. Verdaguer-Casadevall, P. Malacrida, U. Gronbjerg, B. P. Knudsen, A. K. Jepsen, J. Rossmeisl, I. E. Stephens and I. Chorkendorff, *J. Am. Chem. Soc.*, 2012, **134**, 16476-16479.
20. H. Taghinejad, A. A. Eftekhar, P. M. Campbell, B. Beatty, M. Taghinejad, Y. Zhou, C. J. Perini, H. Moradinejad, W. E. Henderson, E. V. Woods, X. Zhang, P. Ajayan, E. J. Reed, E. M. Vogel and A. Adibi, *npj 2D Mater. Appl.*, 2018, **2**, 10.
21. X. T. Wang, T. Ouyang, L. Wang, J. H. Zhong, T. Ma and Z. Q. Liu, *Angew. Chem. Int. Ed.*, 2019, **131**, 13425-13430.
22. C. L. Muhich, V. J. Aston, R. M. Trottier, A. W. Weimer and C. B. Musgrave, *Chem. Mater.* 2016, **28**, 214-226.
23. Y. Liu, X. Hua, C. Xiao, T. Zhou, P. Huang, Z. Guo, B. Pan and Y. Xie, *J. Am. Chem. Soc.*, 2016, **138**, 5087-5092.
24. Y. Liu, C. Xiao, P. Huang, M. Cheng and Y. Xie, *Chem*, 2018, **4**, 1263-1283.
25. J. Zhang, W. Xiao, P. Xi, S. Xi, Y. Du, D. Gao and J. Ding, *ACS Energy Lett.*, 2017, **2**, 1022-1028.
26. Y. Cao, X. Zheng, H. Zhang, J. Zhang, X. Han, C. Zhong, W. Hu and Y. Deng, *J. Power Sources*, 2019, **437**, 226893.
27. P. Ganesan, M. Prabu, J. Sanetuntikul and S. Shanmugam, *ACS Catal.*, 2015, **5**, 3625-3637.
28. L. Guo, J. Deng, G. Wang, Y. Hao, K. Bi, X. Wang and Y. Yang, *Adv. Funct. Mater.*, 2018, **28**, 1804540.
29. K. Liang, L. Li and Y. Yang, *ACS Energy Lett.*, 2017, **2**, 373-390.
30. F. Pan and Y. Yang, *Energy Environ. Sci.*, 2020, **13**, 2275-2309.
31. Y. Yang, H. Fei, G. Ruan and J. M. Tour, *Adv. Mater.*, 2015, **27**, 3175-3180.
32. J. Zhang, Y. Liu, C. Sun, P. Xi, S. Peng, D. Gao and D. Xue, *ACS Energy Lett.*, 2018, **3**, 779-786.
33. Y. Guo, L. Gan, C. Shang, E. Wang and J. Wang, *Adv. Funct. Mater.*, 2017, **27**, 1602699.
34. S. Peng, T. Zhang, L. Li, C. Shen, F. Cheng, M. Srinivasan, Q. Yan, S. Ramakrishna and J. Chen, *Nano Energy*, 2015, **16**, 163-172.
35. K. i. Murai, Y. Suzuki, T. Moriga and A. Yoshiasa, presented at *AIP Conf. Proc.* American Institute of Physics,2007.

36. J. Zhao, M. Konh and A. Teplyakov, *Appl. Surf. Sci.*, 2018, **455**, 438-445.
37. R. F. Blundy and L. L. Shreier, *Corros. Sci.*, 1977, **17**.
38. G. He, W. Zhang, Y. Deng, C. Zhong, W. Hu and X. Han, *Catalysts*, 2017, **7**, 366.
39. L. Guo, Z. Yang, K. Marcus, Z. Li, B. Luo, L. Zhou, X. Wang, Y. Du and Y. Yang, *Energy Environ. Sci.*, 2018, **11**, 106-114.
40. X. Fan, Y. Liu, S. Chen, J. Shi, J. Wang, A. Fan, W. Zan, S. Li, W. A. Goddard and X.-M. Zhang, *Nat. Commun.*, 2018, **9**, 1-11.
41. Y. Xu and M. A. Schoonen, *Am. Mineral.*, 2000, **85**, 543-556.
42. M. Wang, L. Árnadóttir, Z. J. Xu and Z. Feng, *Nanomicro Lett.*, 2019, **11**, 47.
43. M. Wang, B. Han, J. Deng, Y. Jiang, M. Zhou, M. Lucero, Y. Wang, Y. Chen, Z. Yang, A. T. N'Diaye, Q. Wang, Z. J. Xu and Z. Feng, *ACS Appl. Mater. Interfaces*, 2019, **11**, 5682-5686.
44. X. Zhang, Y. Wang, M. Gu, M. Wang, Z. Zhang, W. Pan, Z. Jiang, H. Zheng, M. Lucero and H. Wang, *Nat. Energy*, 2020, **5**, 684-692.
45. Z. Weng, Y. Wu, M. Wang, J. Jiang, K. Yang, S. Huo, X.-F. Wang, Q. Ma, G. W. Brudvig and V. S. Batista, *Nat. Communi.*, 2018, **9**, 1-9.
46. L. Chen, T. Mashimo, C. Iwamoto, H. Okudera, E. Omurzak, H. S. Ganapathy, H. Ihara, J. Zhang, Z. Abdullaeva and S. Takebe, *Nanotechnology*, 2013, **24**, 045602.
47. L. Valério, N. Mamani, A. De Zevallos, A. Mesquita, M. Bernardi, A. Doriguetto and H. De Carvalho, *RSC Adv.*, 2017, **7**, 20611-20619.
48. T. E. de Souza, A. Mesquita, A. O. de Zevallos, F. Beron, K. R. Pirota, P. P. Neves, A. C. Doriguetto and H. B. de Carvalho, *J. Phys. Chem. C*, 2013, **117**, 13252-13260.
49. M. Park, J. Ryu, W. Wang and J. Cho, *Nat. Rev. Mater.*, 2016, **2**, 1-18.
50. Y. Cheng, D. Li, L. Shi and Z. Xiang, *Nano Energy*, 2018, **47**, 361-367.
51. P. Peng, L. Shi, F. Huo, S. Zhang, C. Mi, Y. Cheng and Z. Xiang, *ACS Nano*, 2019, **13**, 878-884.
52. C. Ling, L. Shi, Y. Ouyang, X. C. Zeng and J. Wang, *Nano lett.*, 2017, **17**, 5133-5139.
53. F. Hayee, L. Yu, J. L. Zhang, C. J. Ciccarino, M. Nguyen, A. F. Marshall, I. Aharonovich, J. Vučković, P. Narang, T. F. Heinz and J. A. Dionne, *Nat. Mater.*, 2020, **19**, 534-539.
54. J. P. Locquet, J. Perret, J. Fompeyrine, E. Mächler, J. W. Seo and G. Van Tendeloo, *Nature*, 1998, **394**, 453-456.
55. S. Zhang, B. Ma, X. Zhou, Q. Hua, J. Gong, T. Liu, X. Cui, J. Zhu, W. Guo, L. Jing, W. Hu and Z. L. Wang, *Nat. Communi.*, 2020, **11**, 326.

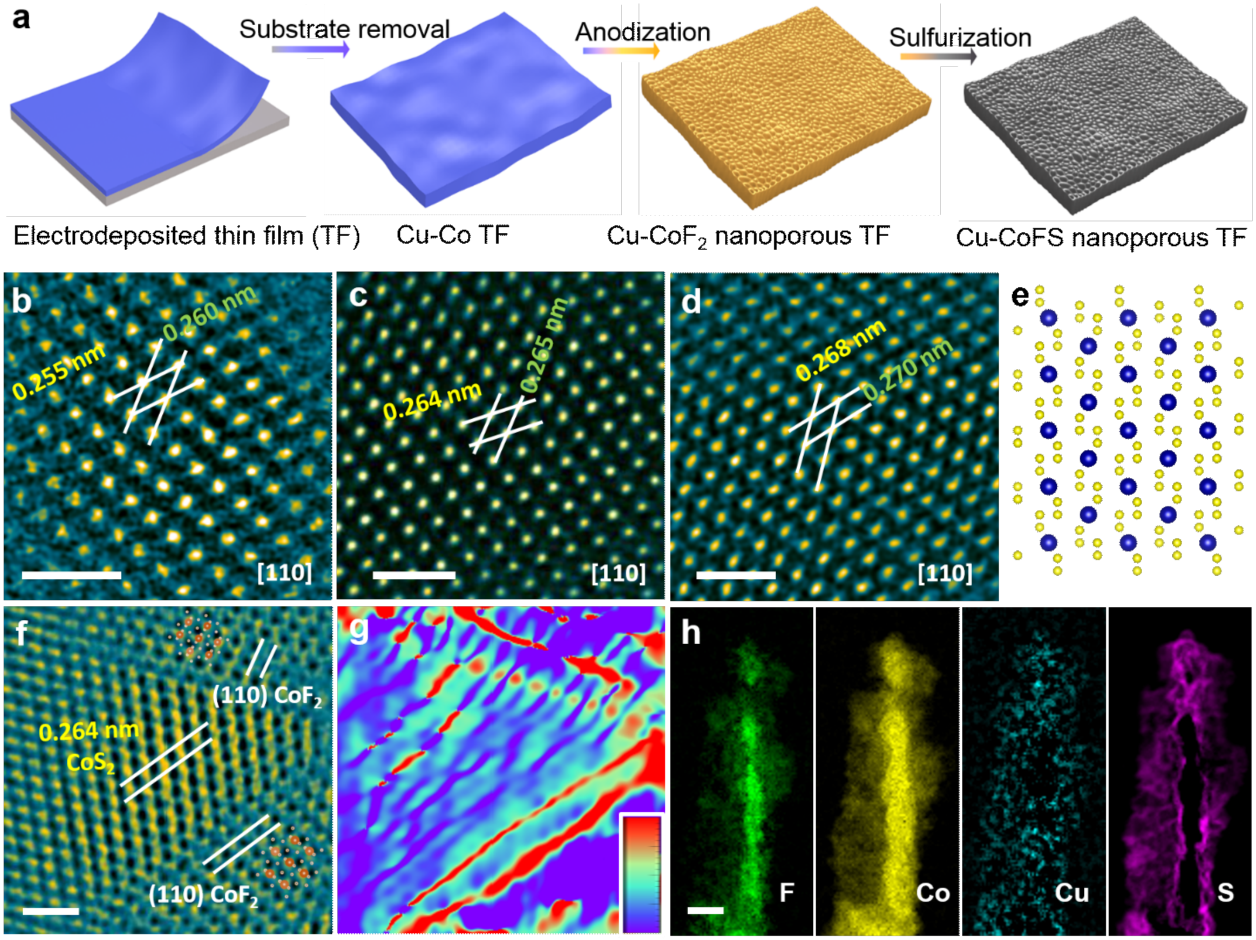

Figure 1. Cu-doping-modulated strained Cu$_x$-CoFS. (a) Schematic of the preparation of Cu$_x$-CoFS nanoporous film. (b-d) HAADF-STEM images of Cu$_{4.42}$-CoFS, Cu$_{6.81}$-CoFS, and Cu$_{11.27}$-CoFS, respectively. Scale bar: 1 nm. (e) Atomic model of CoS$_2$ in Cu$_x$-CoFS. The blue and yellow balls represent Co and S atoms, receptively. (f) HAADF-STEM image and (g) the corresponding geometric phase analysis (GPA) for the lattice strain distribution at the CoF$_2$-CoS$_2$ interface in Cu$_{6.81}$-CoFS. Scale bar: 1 nm. (h) STEM-EELS mapping of the sidewall of the Cu$_{6.81}$-CoFS tubular channels. Scale bar: 50 nm.

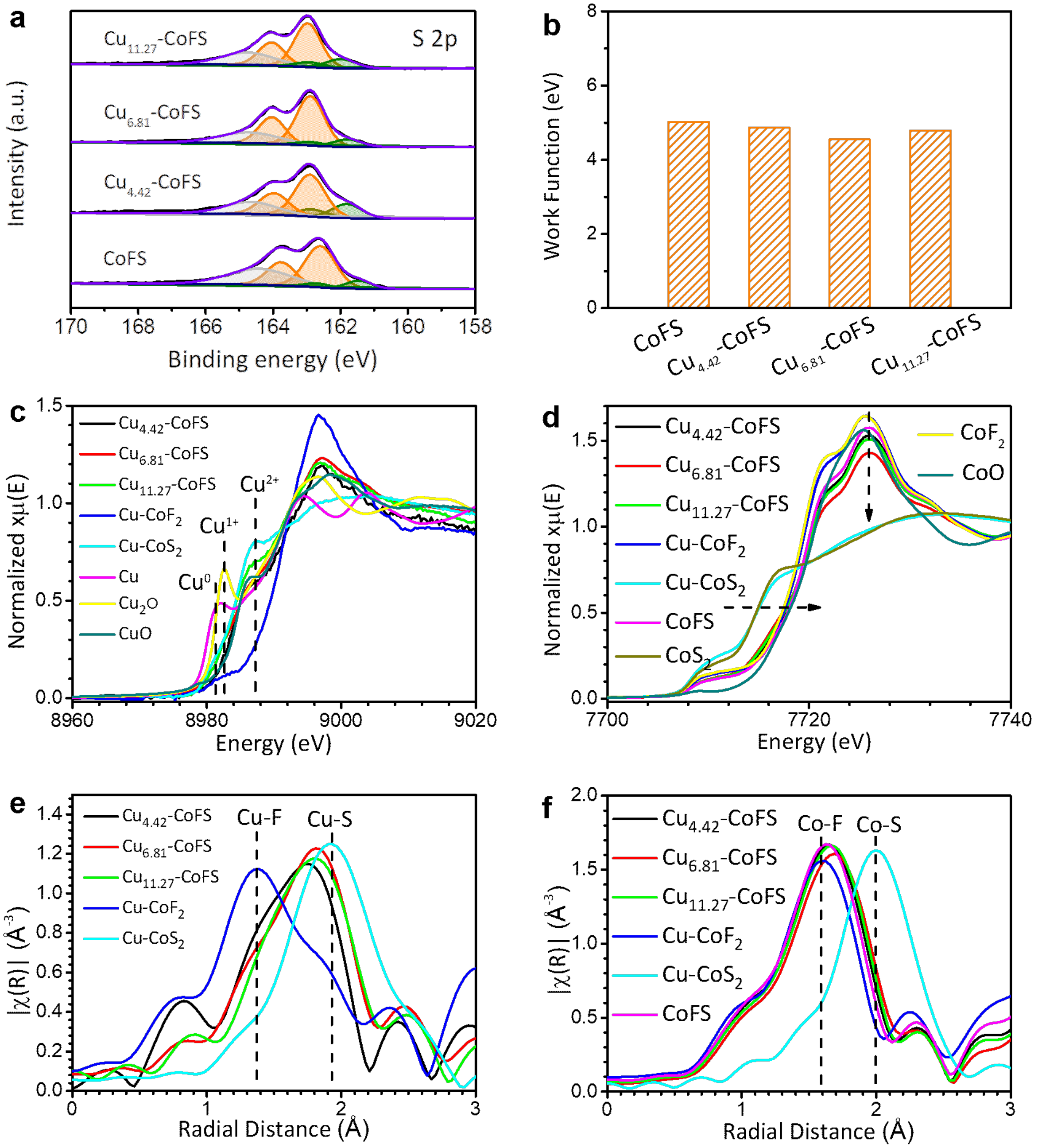

Figure 2. Spectroscopic analyses of the strained Cu_x-CoFS and reference catalysts. (a) High-resolution XPS S2p profiles of Cu_x-CoFS. (b) Work functions of profiles of Cu_x-CoFS. (c, d) Cu K-edge and Co K-edge XANES, respectively. (e, f) Cu K-edge and Co K-edge EXAFS Fourier transform magnitudes (R-space), respectively.

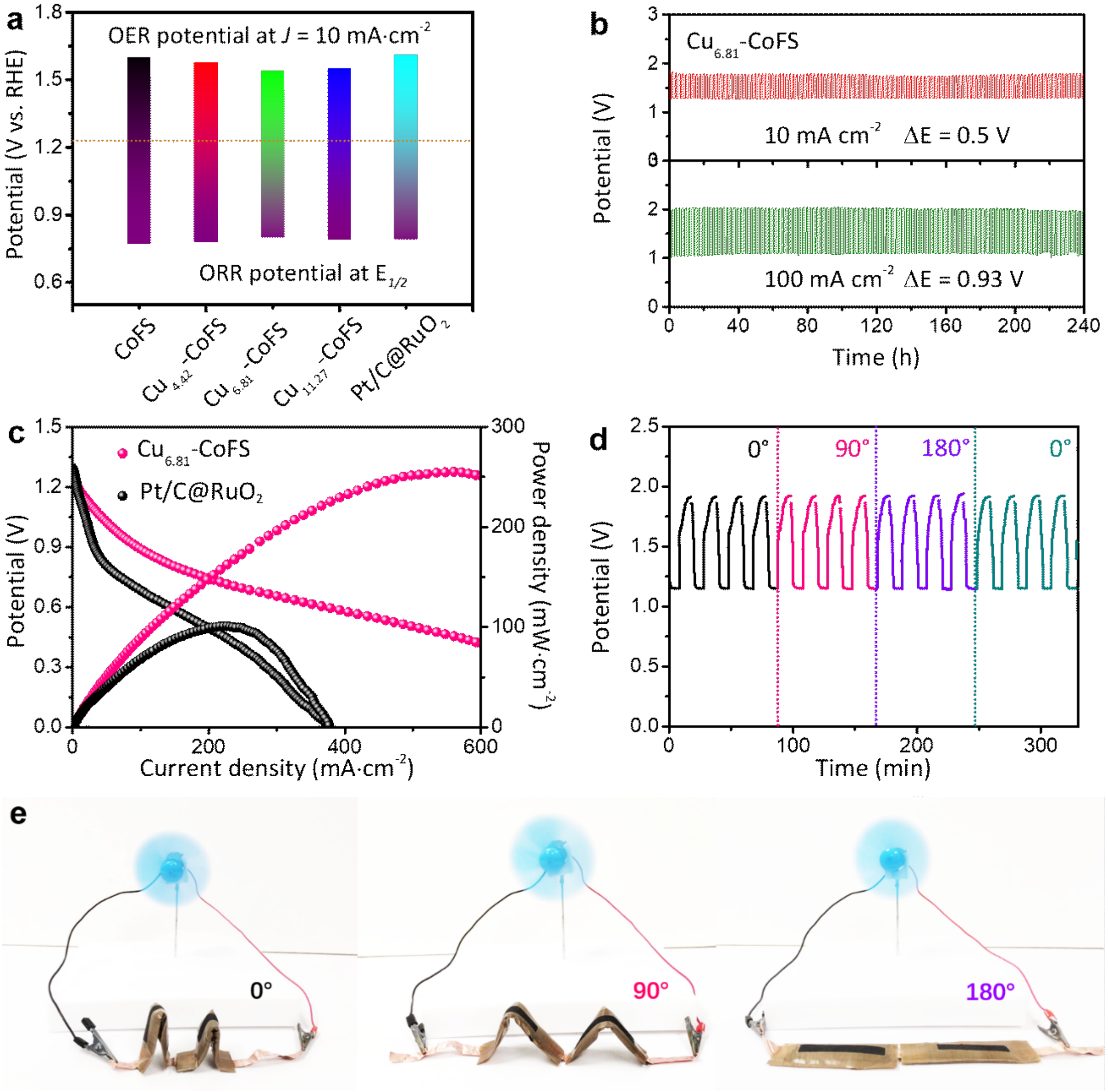

Figure 3. Electrochemical and ZABs performance of $Cu_{6.81}$-CoFS. (a) Bifunctional ORR/OER performance of the catalysts, estimated from the potential difference between OER and ORR. (b) Discharge-charge curves of $Cu_{6.81}$-CoFS at the current density of 5 and 10 mA cm^{-2} in flow cells, successively. (c) Polarization curves of $Cu_{6.81}$-CoFS and Pt/C@RuO_2. (d) Discharge-charge curves of $Cu_{6.81}$-CoFS in foldable ZABs under various bending angles. (e) Digital photographs of the foldable ZABs at different bending angles (Note: 0° and 180° represent the fully-folded and unfolded states, respectively) to drive an electronic fan.

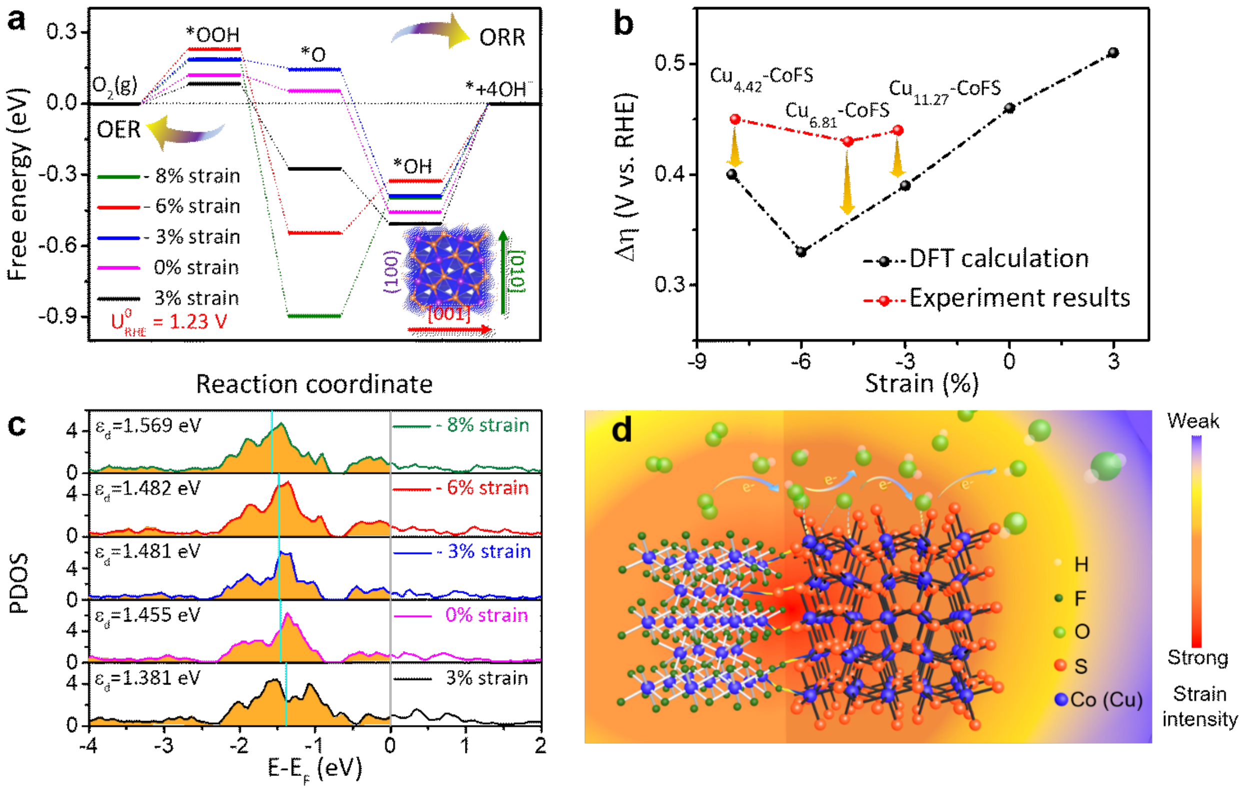

Figure 4. Theoretical understanding of the reaction pathways and mechanism for ORR/OER in the strained catalysts. (a) Calculated ORR/OER free energy diagram at the equilibrium potential (1.23 V vs. RHE) on different strains (e.g., -8%, -6%, -3%, 0%, and 3%. Note the negative ad positive values represent the compressive and tensile strain, respectively). (b) The changes in experimental half-wave potential and theoretical overpotentials as a function of lattice strain. (c) Calculated PDOS for the d band of Co atom in CoS_2(100) facet with different strains. The d band center is marked by the cyan solid line, and the Fermi level is set as zero. (d) Schematic illustration of the reaction pathways for ORR/OER via the four-electron transfer process.